

# Estimation of 3D Left Ventricular Deformation from Echocardiography

Xenophon Papademetris<sup>1</sup> Albert J. Sinusas<sup>2,3</sup>  
Donald P. Dione<sup>3</sup> and James S. Duncan<sup>1,2</sup>

*Yale Image Processing and Analysis Group, Yale University School of Medicine,  
Department of Diagnostic Radiology, PO Box 208042, New Haven, CT  
06520-8042. U.S.A.*<sup>4</sup>

---

## Abstract

The quantitative estimation of regional cardiac deformation from 3D image sequences has important clinical implications for the assessment of viability in the heart wall. Such estimates have so far been obtained almost exclusively from Magnetic Resonance (MR) images, specifically MR tagging. In this paper we describe a methodology for estimating cardiac deformations from 3D echocardiography (3DE). The images are segmented interactively and then initial correspondence is established using a shape-tracking approach. A dense motion field is then estimated using an anisotropic linear elastic model, which accounts for the fiber directions in the left ventricle. The dense motion field is in turn used to calculate the deformation of the heart wall in terms of strain in cardiac specific directions. The strains obtained using this approach in open-chest dogs before and after coronary occlusion, show good agreement with previously published results in the literature. They also exhibit a high correlation with strains produced in the same animals using implanted sonomicrometers. This proposed method provides quantitative regional 3D estimates of heart deformation from ultrasound images.

---

## 1 Introduction

A fundamental goal of many efforts in the cardiac imaging and image analysis communities is to assess the regional function of the left ventricle (LV) of the

---

<sup>1</sup> Departments of Electrical Engineering, Yale University.

<sup>2</sup> Department of Diagnostic Radiology, Yale University.

<sup>3</sup> Department of Medicine, Yale University.

<sup>4</sup> papad@noodle.med.yale.edu

heart. The general consensus is that the analysis of heart wall deformation provides quantitative estimates of the location and extent of ischemic myocardial injury. Regional left ventricular deformation can be determined using all of the principal imaging modalities, including contrast angiography, echocardiography, radionuclide imaging, cine computed tomography (CT), and magnetic resonance (MR) imaging. There have been considerable efforts within the medical image analysis community aimed at estimating this deformation from each of these imaging modalities. Much of the effort has been confined to analysis of two-dimensional images or projections of the heart. Although, recently significant effort has been directed at a more comprehensive analysis of left ventricular deformation in all three dimensions.

Left ventricular deformation can be assessed in three-dimensional space using ECG-gated single photon emission computed tomography (SPECT) [1–7] or positron emission tomography (PET) [8–10]. However, both of these radionuclide methods have a restricted ability to assess left ventricular deformation, secondary to the limited spatial and temporal resolution of these approaches. These radionuclide methods have involved both count-based [1,4,7] and geometry-based approaches [2,3,6].

Cine MR imaging has emerged as a more comprehensive approach to assess myocardial deformation in three-dimensional space [11]. MR imaging offers improved spatial resolution. Unique to cine MR imaging is the ability to track deformation of myocardial tissue within the wall as well as on the endocardial and epicardial surfaces. However, the analysis of mid-wall myocardial deformation requires special cine MR imaging sequences, including MR tissue tagging [12–17] and others, or MR phase contrast velocity imaging [18–21]. While these newer MR approaches offer a comprehensive analysis of regional left ventricular deformation, wide application of MR imaging remains limited by cost and the difficulty in routinely applying these MR approaches to critically ill cardiac patients.

Echocardiography offers significant advantages over both radionuclide imaging and MR imaging. Echocardiographic images can be acquired on critically ill patients in an emergency room or at the patient's bedside in the intensive care unit, and this can be accomplished at a reduced cost. Comprehensive analysis of left ventricular deformation is now feasible using echocardiography, with the advent of newer three-dimensional acquisition systems [22]. Recently, commercial software has become available to automatically assess global and regional left ventricular function [23]. However, these newer automated echocardiographic approaches have not been fully validated. Hence, development of automated analysis of echocardiographic images is attracting an increasing amount of attention in the literature [24–31]. However, none of these methods is capable of estimating dense maps of three-dimensional deformation from echocardiographic images comparable to those obtained from

the analysis of MR tagging images.

In this paper we describe, test and present preliminary validation for an approach to estimate the regional three-dimensional deformation of the left ventricle using echocardiography. We use a biomechanical model to describe the myocardium and shape-based tracking displacement estimates on the endocardial and epicardial walls to generate the initial displacement estimates. These are integrated in a Bayesian estimation framework and the overall problem is solved using the finite element method. This method produces *quantitative regional* 3D cardiac deformation estimates from ultrasound images which up-to now was thought to be only possible using magnetic resonance and especially MR tagging. We validate these estimates by comparing them to invasive measurements performed simultaneously using implanted sonomicrometers. The fast improving quality of ultrasound images with the introduction of harmonic imaging [32] and contrast agents [33] should make it possible to obtain even more accurate estimates of 3D left ventricular deformation in the future.

## 2 Our Approach

We estimate a dense displacement field within a Bayesian estimation framework which consists of a data term and a model term. These are described in sections 2.1 and 2.2 respectively. The data term captures the image-derived information about the problem. We segment the images interactively and then proceed to extract initial displacement estimates using a shape-tracking approach. We then model the noise in these estimates using a Gaussian noise model. The model term captures our prior beliefs about the nature of the displacement field. Since the left ventricle is a single deforming body, we expect the displacements of neighboring points to be related. We capture this relationship using a biomechanical model which is, in turn, used to generate a prior probability density function for the displacement field. Our approach that incorporates a biomechanical model has the advantages of having no arbitrarily set weights and of allowing us to take advantage of forward modeling efforts in the biomechanics literature, see for example the collections in [34,35].

### 2.1 Obtaining Initial Displacement Data

#### 2.1.1 Image Acquisition

The images were acquired using an HP Sonos 5500 Ultrasound System with a 3D transducer (Transthoracic OmniPlane 21349A (R5012)). The 3D-probe was placed at the apex of the left-ventricle of an open-chest dog using a small

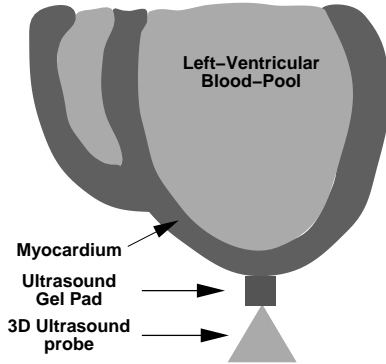


Fig. 1. Image acquisition geometry.

ultrasound gelpad (Aquaflex) as a standoff as shown in figure 1. Each acquisition consisted of 13–17 frames per cardiac cycle depending on the heart rate. The angular slice spacing was 5 degrees resulting in 36 image slices for each frame. For validation purposes we also implanted arrays of sonomicrometer crystals [36,37] at two positions in the left ventricle.

### 2.1.2 Image Segmentation

The endocardial and epicardial surfaces were extracted interactively using a software platform [38] originally developed for MR image data and subsequently modified to allow for the different geometry and image characteristics of ultrasound. For the automated part of the segmentation, for each image slice, we used an integrated deformable boundary method whose external energy function consisted of a standard intensity gradient term and a texture-based term similar to that proposed by Chakraborty [39]. In our approach, however, the contours were parameterized using B-splines [40] to allow for easy interaction. Clearly detecting the epicardium is the hardest of the two tasks. At this point we are relying on operator intervention and correction of the automatic algorithm to ensure accurate segmentation.

The texture model tries to classify each pixel in one of three classes (blood pool, myocardium, region outside the epicardium) by modeling each class using texture parameters derived from the work of Manjunath [41]. The mean values of these parameters for each class are set interactively by having the user click on one point in each of the three regions. Then the variability of these parameters in each class is modeled as a normal distribution assuming equal variances for all the classes. A first-order Gaussian Markov Random Field (GMRF) model is used to model the class-label for each pixel. The GMRF combines the likelihood of belonging to a class as specified by the texture parameters with a degree of regional smoothness in the classification. A more detailed description can be found in [42].

The overall framework produced reasonable results as shown in figures 2 and

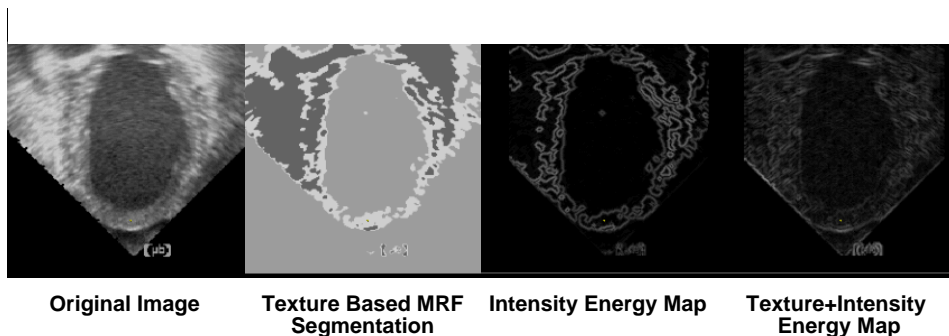


Fig. 2. External Energy Functions for intensity and intensity+texture snakes. Note that the intensity only energy function is very noisy inside the left-ventricular blood-pool which creates many local minima for the deformable contour. The use of the texture eliminates most of these minima.

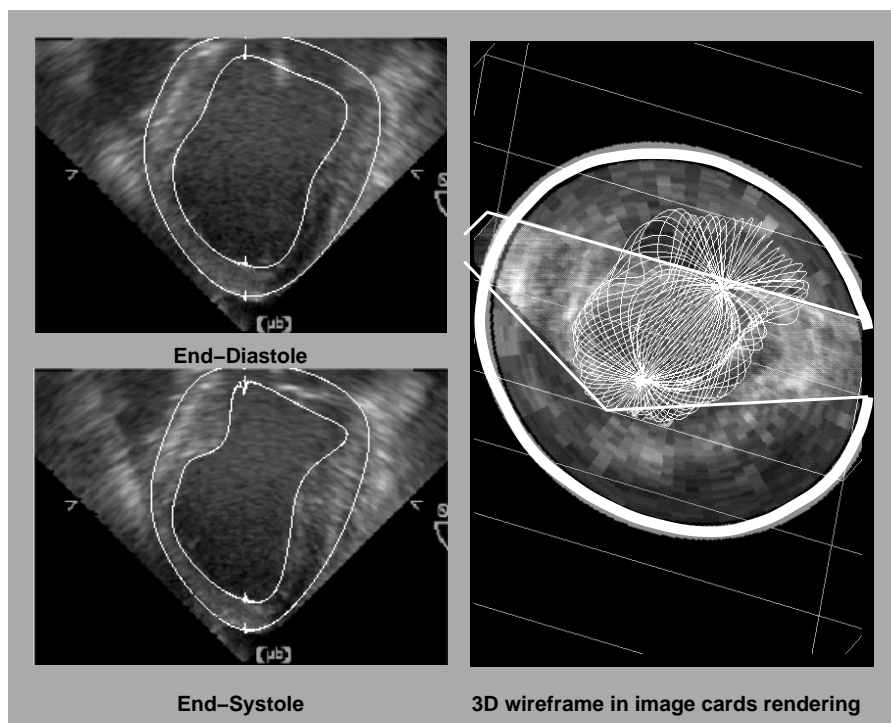


Fig. 3. Left: Images and superimposed extracted contours. Only two of the eight frames are shown. Right: 3D rendering showing all the wire-frame contours superimposed on a long axis (original) and a short-axis (interpolated) image slices.

3. There is clearly room for improvement in this approach, as we are not yet taking advantage of the temporal coherency in the spatial position of surfaces across times. The potential benefits of using such constraints is demonstrated in a number of papers, including [28,29,31]. We are also currently looking into more sophisticated techniques for generating the external energy maps, including those suggested by Mulet-Parada [43].

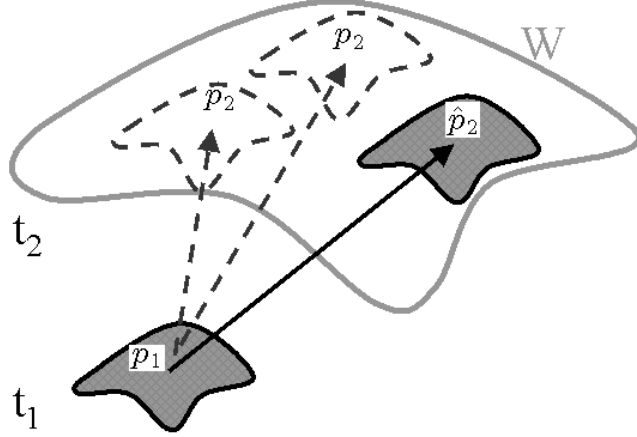


Fig. 4. Example of the shape-tracking approach. The goal here is to map points on the original surface to points on the final surface. For a point  $p_1$  on the original surface, we define a search window  $W$  on the final surface which contains all plausible corresponding points. Then the point  $p_2$  in  $W$  which has the most similar shape-properties to  $p_1$  is selected as the candidate match point. The distance function for shape-similarity is based on the difference in principal curvatures.

### 2.1.3 Shape-Tracking Displacement Estimates

In this work, the original displacements on the surfaces of the myocardium were obtained by using the shape-tracking algorithm whose details were presented in [44,42]. The method tries to track points on successive surfaces using a shape similarity metric which tries to minimize the difference in principal curvatures and was validated using implanted markers [44].

For example, consider point  $p_1$  on a surface at time  $t_1$  which is to be mapped to a point  $p_2$  on the deformed surface at time  $t_2$ , as shown in figure 4. First, a search is performed in a physically plausible region  $W$  on the deformed surface and the point  $\hat{p}_2$  which has the local shape properties closest to those  $p_1$  is selected. The shape properties here are captured in terms of the principal curvatures  $\kappa_1$  and  $\kappa_2$ . The distance measure used is the bending energy required to bend a curved plate or surface patch to a newly deformed state. This is labeled as  $d_{be}$  and is defined as:

$$d_{be}(p_1, p_2) = \left( \frac{(\kappa_1(p_1) - \kappa_1(p_2))^2 + (\kappa_2(p_1) - \kappa_2(p_2))^2}{2} \right) \quad (1)$$

The displacement estimate vector for each point  $p_1$ ,  $u_1^m$  is given by

$$u_1^m = \hat{p}_2 - p_1 \quad , \quad \hat{p}_2 = \arg \min_{p_2 \in W} [d_{be}(p_1, p_2)]$$

**Confidence Measures in the match:** The bending energy measures for all the points inside the search region  $W$  are recorded as the basis to measure the *goodness* and *uniqueness* of the matching choice. The value of the minimum bending energy in the search region between the matched points indicates the goodness of the match. Denote this value as  $m_g$ , we have the following measure for matching goodness:

$$m_g(p_1) = d_{be}(p_1, \hat{p}_2) \quad (2)$$

On the other hand, it is desirable that the chosen matching point is a unique choice among the candidate points within the search window. Ideally, the bending energy value of the chosen point should be an outlier (much smaller value) compared to the values of the rest of the points. If we denote the mean values of the bending energy measures of all the points inside window  $W$  except the chosen point as  $\bar{d}_{be}$  and the standard deviation as  $\sigma_{be}^d$ , we define the uniqueness measure as:

$$m_u(p_1) = \frac{d_{be}(p_1, \hat{p}_2)}{\bar{d}_{be} - \sigma_{be}^d} \quad (3)$$

This uniqueness measure has a high value if the bending energy of the chosen point is small compared to some smaller value (mean minus standard deviation) of the remaining bending energy measures. Combining these two measures together, we arrive at one *confidence measure*  $c^m(p_1)$  for the matched point  $\hat{p}_2$  of point  $p_1$ :

$$c^m(p_1) = \frac{1}{k_{1,g} + k_{2,g}m_g(p_1)} \times \frac{1}{k_{1,u} + k_{2,u}m_u(p_1)} \quad (4)$$

where  $k_{1,g}$ ,  $k_{2,g}$ ,  $k_{1,u}$ , and  $k_{2,u}$  are scaling constants for normalization purposes. We normalize the confidences to lie in the range 0 to 1.

**Modeling the initial displacement estimates:** Given a set of displacement vector measurements  $u^m$  and confidence measures  $c^m$  we model these estimates probabilistically by assuming that the noise in the individual measurements is normally distributed with zero mean and a variance  $\sigma^2 = \frac{1}{c^m}$ . In addition, we assume that the measurements are uncorrelated. Given these assumptions we can write the measurement probability for each point as:

$$p(u^m|u) = \frac{1}{\sqrt{2\pi\sigma^2}} e^{-\frac{(u-u^m)^2}{2\sigma^2}} \quad (5)$$

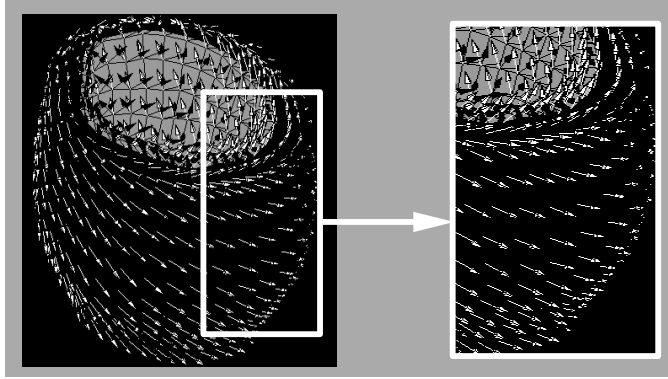


Fig. 5. Fiber direction in the left ventricle as defined in Guccione [45].

## 2.2 Modeling the myocardium

The left-ventricular myocardium is modeled using using a transversely isotropic linear elastic model which allows us to incorporate information about the preferential stiffness of the tissue along fiber directions from Guccione [45]. These fiber directions are shown in figure 5. The model described in terms of an internal or strain energy function of the form:

$$W = e^t C e \quad (6)$$

where  $e$  is the vector form of the strain tensor  $\epsilon$  (see next section),  $e^t$  is the transpose of  $e$  and  $C$  is the  $6 \times 6$  matrix containing the elastic constants which define the material properties. This is described in more detailed in continuum mechanics textbooks such as Malvern [46].

**Deformation and Strain:** Consider a body  $B(0)$  which after time  $t$  moves and deforms to body  $B(t)$  as shown in figure 6. A point  $X$  on  $B(0)$  goes to a point  $x$  on  $B(t)$  and the transformation gradient  $F$  is defined as  $dx = FdX$ . The deformation is expressed in terms of the strain tensor  $\epsilon$ . Because the deformations to be estimated in this work are larger than 5%, we use a finite strain formulation implemented using a logarithmic strain  $\epsilon^L$ , which is defined as:  $\epsilon^L = \ln\sqrt{F \cdot F^t}$ . Since the strain tensor is a  $3 \times 3$  symmetric 2nd-rank tensor (matrix), we can re-write it in vector form as,  $e = [\epsilon_{11} \ \epsilon_{22} \ \epsilon_{33} \ \epsilon_{12} \ \epsilon_{13} \ \epsilon_{23}]^t$ . This enables us to express the tensor equations in a more familiar matrix notation.

**Strain Energy Function:** The mechanical model can be defined in terms of a strain energy function. The simplest useful continuum model in solid mechanics is the linear elastic one which is of the form:  $W = e^t C e$  where  $C$  is a  $6 \times 6$  matrix and defines the material properties of the deforming body and  $e$  is the vector form of the strain tensor. The simplest model is the isotropic

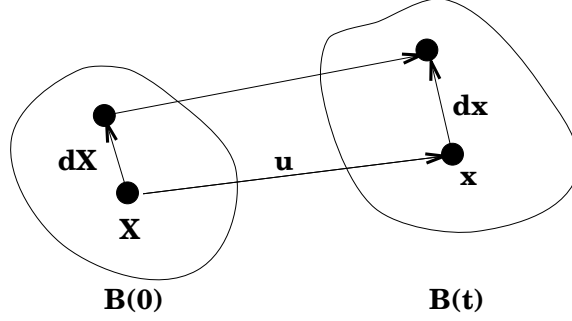


Fig. 6. Geometry of deformation. In this case a body  $B(0)$  goes to a body  $B(t)$ . The deformation operator  $F$  is defined as  $dx = FdX$ .

linear elastic model used widely in the image analysis literature [19,13]. In this case the matrix  $C$  takes the form:

$$C^{-1} = \frac{1}{E} \begin{bmatrix} 1 & -\nu & -\nu & 0 & 0 & 0 \\ -\nu & 1 & -\nu & 0 & 0 & 0 \\ -\nu & -\nu & 1 & 0 & 0 & 0 \\ 0 & 0 & 0 & 2(1+\nu) & 0 & 0 \\ 0 & 0 & 0 & 0 & 2(1+\nu) & 0 \\ 0 & 0 & 0 & 0 & 0 & 2(1+\nu) \end{bmatrix} \quad (7)$$

where  $E$  is the Young's modulus that is a measure of the stiffness of the material and  $\nu$  is the Poisson's ratio which is a measure of incompressibility.

In this work, the left ventricle of the heart is specifically modeled as a transversely elastic material to account for the preferential stiffness in the fiber direction. This is an extension of the isotropic linear elastic model which allows for one of the three material axis to have a different stiffness from the other two. In this case the matrix  $C$  takes the form:

$$C^{-1} = \begin{bmatrix} \frac{1}{E_p} & \frac{-\nu_p}{E_p} & \frac{-\nu_{fp}}{E_f} & 0 & 0 & 0 \\ \frac{-\nu_p}{E_p} & \frac{1}{E_p} & \frac{-\nu_{fp}}{E_f} & 0 & 0 & 0 \\ \frac{-\nu_{fp}E_f}{E_p} & \frac{-\nu_{fp}E_f}{E_p} & \frac{1}{E_f} & 0 & 0 & 0 \\ 0 & 0 & 0 & \frac{2(1+\nu_p)}{E_p} & 0 & 0 \\ 0 & 0 & 0 & 0 & \frac{1}{G_f} & 0 \\ 0 & 0 & 0 & 0 & 0 & \frac{1}{G_f} \end{bmatrix} \quad (8)$$

where  $E_f$  is the fiber stiffness,  $E_p$  is cross-fiber stiffness and  $\nu_{fp}, \nu_p$  are the corresponding Poisson's ratios and  $G_f$  is the shear modulus across fibers. ( $G_f \approx E_f/(2(1+\nu_{fp}))$ ). If  $E_f = E_p$  and  $\nu_p = \nu_{fp}$  this model reduces to

the more common isotropic linear elastic model. The fiber stiffness was set to be 3.5 times greater than the cross-fiber stiffness [45]. The Poisson's ratios were both set to 0.4 to model approximate incompressibility.<sup>5</sup>

In using a linear elastic model we lose the ability to capture the progressive hardening of the left ventricular myocardium as the strain increases, unlike for example the non-linear models used by Guccione et al [45]. This is mitigated by the fact that the estimation is done on a frame by frame basis hence the degree of the hardening would be small.

**A probabilistic description of the model:** As previously demonstrated by Geman and Geman [48] and applied to medical image analysis problems [49,50] there is a correspondence between an internal energy function and a Gibbs probability density function. If the mechanical model is described in terms of an internal energy function  $W(C, u)$ , where  $C$  represents the material properties and  $u$  the displacement field, then we can write an equivalent prior probability density function  $p(u)$  (see equation 10) of the Gibbs form [48]:

$$p(u) = k_1 \exp(-W(C, u)) \quad (9)$$

where  $k_1$  is a normalization constant.

The Markov random field (MRF) then can be thought of as the probabilistic analog of the continuum mechanical model. There are two interesting similarities: (i) Both can be defined using energy functions and (ii) the energy functions at any given point are functions only of the values of that point and its immediate neighbors. In the case of the MRF point (ii) comes from the fact that the the Gibbs probability density function is often defined on first and/or second order cliques which are very local neighborhoods of the point. So if the displacement field is modeled as a MRF, the probability of the displacement of a given point  $p$  effectively only depends on the displacement of its neighbors. In the case of the mechanical model described using a strain energy function, the value of the internal energy function, which via exponentiation in equation (9) becomes the probability density function, at a given point depends only on the local strains. These local strains are only dependent on the displacements of the neighbors of the point and not on the displacements of the whole volume.

The expression of the mechanical model as a MRF allows us to solve the problem within the Bayesian estimation framework. This has the advantage of

---

<sup>5</sup> The value of 0.4 was chosen to model approximate incompressibility. Experience shows that using values greater than 0.4 often causes numerical problems such as mesh locking [47]. Also the myocardium is only approximately incompressible.

allowing us to model the noise in the displacement estimates probabilistically and still maintaining the description of the model in the language of continuum mechanics.

### 2.3 Integrating the Data and Model Terms

Having defined both the data term (equation 5) and the model term (equation 9) as probability density functions we naturally proceed to write the overall problem in a Bayesian estimation framework. Given a set of noisy input displacement vectors  $u^m$ , the associated noise model  $p(u^m|u)$  (data term) and a prior probability density function  $p(u)$  (model term), find the best output displacements  $\hat{u}$  which maximize the posterior probability  $p(u|u^m)$ . Using Bayes' rule we can write.

$$\hat{u} = \arg \max_u p(u|u^m) = \arg \max_u \left( \frac{p(u^m|u)p(u)}{p(u^m)} \right) \quad (10)$$

The prior probability of the measurements  $p(u^m)$  is a constant once these measurements have been made and therefore drops out of the minimization process. In this expression we also note that there is an undefined constant. This is the scaling factor that translates the stiffness of the mechanical model to the effective variance of its equivalent probability density function  $p(u)$ . This constant essentially translates stiffness which is measured in Pascals to confidence in the model which is measured in pixels. The value of this constant sets the relative weight of the data term to the model term. We set this adaptively to be as large as possible (which pushes the optimum towards the data side) subject to solution convergence. In this way we make the following assumption: the best solution is the one which adheres as much as possible to initial estimate of the displacement field but still results in a connected solid. Convergence fails when the Jacobian of the deformation field<sup>6</sup> becomes singular. In this case we lower the value of this weight to produce a smoother displacement field.

**Model bias and correction:** We also note that the mechanical model prior is generated by a passive biomechanical model, that is one which does not capture the active deformation of the left ventricle. This model has a major weakness in that it penalizes all deformations. This model could be thought in some sense as having a mean of zero strain and a variance proportional to the reciprocal of the stiffness. It will tend to underestimate the deformation and hence the strain. As a certain amount of deformation *does occur* the use of this

---

<sup>6</sup> The Jacobian of the deformation is the matrix  $F$  defined in figure 6.

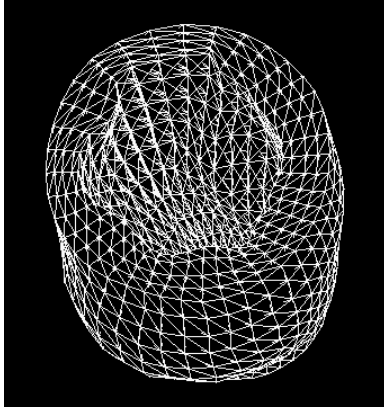


Fig. 7. A 3D Mesh generated by interpolating and filling between the endocardial and epicardial boundaries.

model results in an underestimation of the deformation using our approach. A solution to this problem is to incorporate a model of active contraction within the prior, and this is a subject of on-going research within our group (again see [42].) At this point the problem is dealt with by forcing the nodes which lie on the endocardial and epicardial surfaces at time  $t$  to lie on the segmented surfaces at the time  $t + 1$ . This corrects for the bias in the estimates of the deformation for those components of the deformation which are perpendicular to the endocardial and epicardial surfaces. The bias in the estimation of deformation parallel to the surfaces remains.

#### 2.4 Numerical Solution

Taking logarithms in equation (10) and differentiating with respect to the displacement field  $u$  results in a system of partial differential equations, which we solve using the finite element method [51]. The first step in the finite element method is the division or tessellation of the body of interest into elements; these are commonly tetrahedral or hexahedral in shape. Once this is done, the partial differential equations are written down in integral form for each element, and then the integral of these equations over all the elements is taken to produce the final set of equations. For more information one is referred to standard textbooks such as Bathe [51]. The final set of equations is then solved to produce the output set of displacements. In our case the myocardium is divided into approximately 2,500 hexahedral elements, using a custom mesh generation algorithm described in [42]. A solid mesh of one of the hearts is shown in figure 7.

For each frame between end-systole (ES) and end-diastole (ED), a two step problem is posed: (i) solving equation (10) normally and (ii) adjusting the position of all points on the endocardial and epicardial surfaces so they lie

on the endocardial and epicardial surfaces at the next frame using a modified nearest-neighbor technique and solving equation (10) once more using this added constraint. This ensures that there is a reduction in the bias in the estimation of the deformation.

### 3 Experimental Procedure

**Animal Experiments:** To evaluate the efficacy of using image-derived *in vivo* deformation estimates to measure regional LV function we conducted experiments on fasting, anesthetized, open chest, adult mongrel dogs with approval of the Yale University Animal Care and Use Committee. In this preliminary work, we report results from four animals. The 3DE images were obtained either before (D1 and D2) or after occlusion of the left anterior descending coronary artery (D3 and D4), using the procedure described in section 2.1.1. Coronary occlusion created an area of dysfunction which we call the risk area. Also regional blood flow in the myocardium was determined using a radio-labeled microsphere technique. Here, radioactively labeled microspheres were injected into the left atrium and reference blood samples were drawn from the femoral arteries. Regional myocardial blood flow was calculated using a method previously described in [52]. The blood flow measurements are used to identify the risk area and play no further role in this work. Further we implanted sonomicrometers (Sonometrics Corporation, London Ontario, Canada) at two regions in the myocardium, as shown in the schematic in figure 11(left). We obtain highly accurate invasive measures of the deformation from the analysis of implanted sonomicrometers. Sonomicrometer derived regional strains were considered to be the *gold standard*.

**Image Analysis:** The images were segmented interactively and the surfaces sampled to 0.5 voxel resolution, at which point curvatures were calculated and the shape-tracking algorithm was used to generate initial displacement estimates. The heart wall was divided into 2500 hexahedral elements and the anisotropic linear elastic model was used to regularize the displacements. A commercial finite element solver ABAQUS [53] was used to solve the resulting equations. The computational time after the segmentation was of the order of 3-4 hrs/dog (depending on the heart rate and hence the number of image frames) on a Silicon Graphics Octane with an R10000 195 MHz processor and 128 MB RAM.

**Strain Analysis:** For the purpose of analyzing the results, the left-ventricle of the heart was divided into 4 cross-sectional slices, slice 1 being at the apex

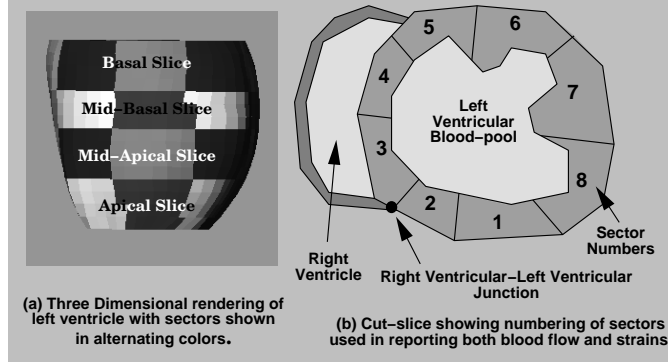


Fig. 8. Division of a slice of the heart for the purpose of reporting results. Each sector consists of approximately 75 elements in the finite element mesh.

of the ventricle and number 4 being at the base of the ventricle towards the valve plane. Each slice was further subdivided into 8 sectors, as shown in figure 8(b). A sector was labeled as being in the risk area if the endocardial microsphere flow was less than  $0.25ml/min/g$ . The normal region was defined by 5 transmural sectors located in the posterior lateral wall at the base of the heart (sectors 5,6,7 of the basal slice and sectors 6,7 of the mid-basal slice). We report the average of radial(RR), circumferential(CC) and longitudinal(LL) strains for the risk areas and the normal regions.<sup>7</sup>

## 4 Results

The potential of our methodology is illustrated in figure 9, which shows a cut through our tracked 3D mesh overlaid on a slice through the original 3DE image data over time. This could be seen as a form of software-derived, 3DE-based “tissue tagging” somewhat in the sense of MR tagging. Note the spreading grid lines near the endocardium on the right as the LV thickens from enddiastole to endsystole.

The quantitative results are summarized in Table 1. Function in the risk area, which was independently defined by microsphere flow, was markedly reduced compared to non-affected regions and the control normal animal. The radial strain is notably smaller in the risk area after coronary occlusion. The circumferential strain becomes less negative also indicating a loss of function. There was a small decrease in the longitudinal strain as well. The progressive

<sup>7</sup> Given a strain tensor  $\epsilon_1$  in a coordinate frame  $c_1$  (e.g.  $x, y, z$ ) we can map it to a new coordinate frame  $c_2$  (e.g.  $r, c, l$ ) by use of a rotation matrix  $R$ . If  $R : c_1 \mapsto c_2$ , then the strain transformation is done as:  $\epsilon_2 = R\epsilon_1R^t$ . In this way we can rotate the strain tensor to line up with directions of interest. We also note that the principal strains are the eigenvalues of the  $3 \times 3$  strain tensor and are invariant to changes in the coordinate frame.

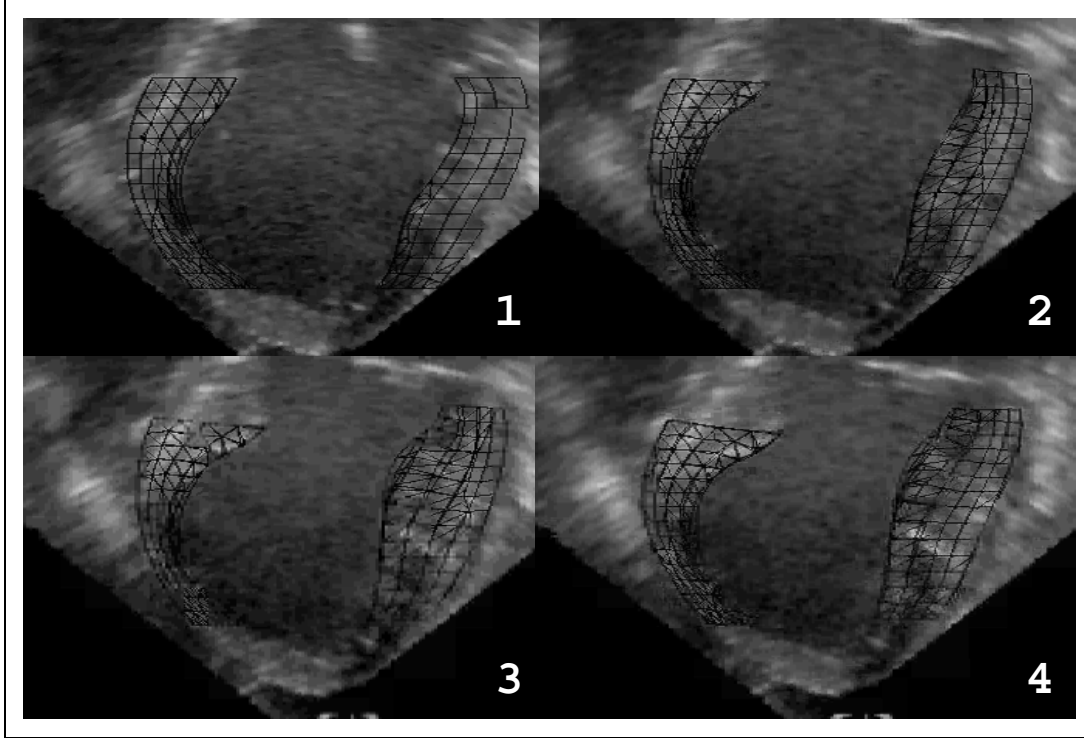


Fig. 9. “3DE-tissue-tagging”- a slice through a 3D visualization with the algorithm-driven deforming mesh overlaid on one slice through a 3DE dataset at four time points between ED and ES. This demonstrates the output of the algorithm which tries to follow (or tag) material points in time, similar to the Magnetic Resonance Tagging approach. Note that thickening (or radial strain) increases from the epicardium to the endocardium as expected. There is also an infarct region in the left half of the image which exhibits bulging instead of contraction. See also the accompanying movie file `papad1.mov`.

Study	D1	D2	D3	D4
Normal Radial Strain	17.7	13.8	22.4	17.2
Normal Circumferential Strain	-13.4	-13.1	-8.4	-12.4
Normal Longitudinal Strain	-4.3	-3.2	-3.4	-3.1
Risk Area Radial Strain	n/a	n/a	-4.3	-13.7
Risk Area Circumferential Strain	n/a	n/a	1.9	-7.3
Risk Area Longitudinal Strain	n/a	n/a	-0.7	-2.0

Table 1

Summary of results for four animal studies. There was no risk area in studies D1 and D2 as the 3DE images, in these cases, were obtained before coronary occlusion.

development of regional radial and circumferential strains for ‘D3’ is shown in figure 10.

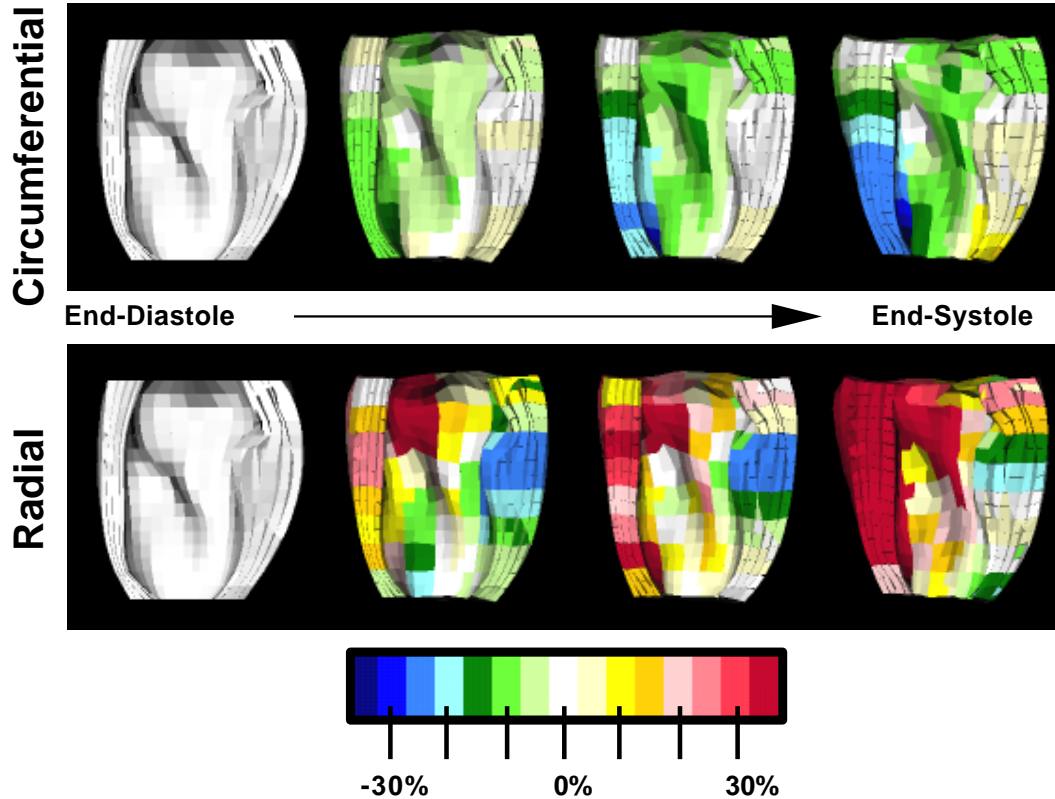


Fig. 10. A long-axis cut-away sectional view of the left ventricle showing circumferential(top) and radial(bottom) strain development in a dog following left anterior descending coronary artery occlusion (on the lower right half of the heart). Note the normal behavior in the left half of the heart. There was positive radial strain (thickening) and negative circumferential strain (shortening) as we move from End Diastole to End Systole. The lower right half of the heart where the affected region was located showed almost the opposite behavior, as expected. See also the accompanying movies [papad2.mov](#) and [papad3.mov](#).

Croisille [54] reported similar values (Radial= $23.2 \pm 1.9\%$ , Circum= $-10.5 \pm 2.0\%$  and Long= $-7.5 \pm 1.0\%$ ) for strains in the normal regions of dog hearts using three-dimensional tagged MRI. However, they observed smaller reductions in strains post-occlusion, which can be attributed to coronary reperfusion in their model and significantly delayed imaging after the occlusion (2 days later as opposed to 15-20 minutes in our case). This probably allowed for partial recovery of function in the risk region.

## 5 Validation using Implanted Sonomicrometers.

In an effort to obtain an independent source of *in vivo* strain values for validation of image-derived strains, we have developed an independent approach for strain measurement using cubic arrays of sonomicrometers implanted in

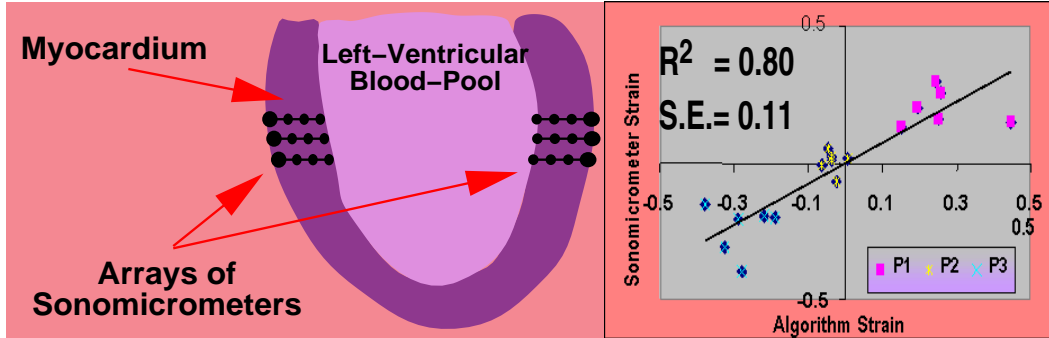


Fig. 11. 3DE Algorithm-Derived Strains vs. Sonomicrometer-derived Strains. Scatter plot of principal strains derived from  $N=3$  3DE studies using the algorithm vs. same strains derived from sonomicrometer arrays (12 crystals in each cluster) at two positions in the Left Ventricular wall. Note the high correlation between the two sets of strain values ( $r^2 = .80$ ).

the canine LV myocardium (see details in [36]). The efficacy of this technique was illustrated by additional work [37] that showed that the distances obtained with sonomicrometers compared favorably ( $r = 0.992$ ) with those obtained using the more established technique of tracking implanted bead displacements using biplane radiography.

We then compared our image-derived strains to concurrently-estimated sonomicrometer derived strains at several positions in the LV myocardium in the same dogs. The sonomicrometers were located visually from the images and the two nearest sectors of algorithm-derived strains were selected for comparison purposes. The comparison of the principal strain components in two separate regions for a set of 3 studies (the sonomicrometer data was not available for study ‘D4’) showed a strong correlation ( $r^2 = 0.80$ ). Here we compare the principal strains as it is difficult to estimate the cardiac specific directions in the case of the sonomicrometer data. A scatter plot of algorithm-derived principal strains versus sonomicrometer derived principal strains is shown in figure 11.

This validation is still in a preliminary stage and we hope in the future, to also validate strain patterns which are not fully averaged across the wall.

## 6 Conclusions

In this work we have demonstrated that estimates of 3D cardiac deformation can be obtained from ultrasound images. These estimates are generally consistent with values reported in the literature. Further, we validate such estimates of regional deformation directly by comparing them to strains measured concurrently from implanted sonomicrometers. While many problems remain to

be solved, such as improving and speeding up the segmentation process, we are confident that this approach has the potential to make 3DE a potential source of images for the comprehensive estimation of 3D cardiac deformation.

## Movies

There are three movies included with this paper. The first movie, `papad1.mov` corresponds to figure 9. The second and third movies, `papad2.mov` and `papad3.mov`, correspond to the top and bottom parts of figure 10 respectively.

## Acknowledgments

The first author would also like to thank professors Turan Onat and Gary Povirk from the Department of Mechanical Engineering at Yale University for many useful discussions. Additional thanks to Farah Janzad, David Meoli, Jason Soares and Jennifer Hu for their help with segmenting the images, processing the sonomicrometer data, tissue processing and surgical preparation respectively. We would like to acknowledge support from the National Institutes of Health under grant NIH-NHLBI RO1-HL44803 and the American Heart Association (Connecticut Affiliate) under grant 9850014T. We would also like to thank Agilent Technologies (formerly part of Hewlett Packard), and especially Dr Karl Thiele, for providing the HP Sonos 5500 Ultrasound System used to acquire the 3DE Images.

## References

- [1] M. Y. Shen, Y. Liu, A. Sinusas, R. Fetterman, W. Bruni, O. Drozhinin, B. Zaret, F.J.Wackers, Quantification of regional myocardial wall thickening on electrocardiogram-gated spect imaging., *Journal of Nuclear Cardiology* 6(6) (1999) 583–95.
- [2] E. Cwajg, J. Cwajg, Z. He, W. Hwang, F. Keng, S. F. Nagueh, M. Verani, Gated myocardial perfusion tomography for the assessment of left ventricular function and volumes: comparison with echocardiography., *Journal of Nuclear Medicine* 40(11) (1999) 1857–65.
- [3] T. L. Faber, C. Cooke, R. Folks, J. Vansant, K. Nichols, E.G.DePuey, R. Pettigrew, E. Garcia, Left ventricular function and perfusion from gated spect perfusion images: an integrated method., *Journal of Nuclear Medicine* 40(4) (1999) 650–9.

- [4] D. Calnon, R. J. Kastner, W. Smith, D. Segalla, G. Beller, D. Watson, Validation of a new counts-based gated single photon emission computed tomography method for quantifying left ventricular systolic function: comparison with equilibrium radionuclide angiography., *Journal of Nuclear Cardiology* 4(6) (1997) 464–71.
- [5] D. Berman, G. Germano, Evaluation of ventricular ejection fraction, wall motion, wall thickening, and other parameters with gated myocardial perfusion single-photon emission computed tomography., *Journal of Nuclear Cardiology* 4(2 Pt 2) (1997) S169–71.
- [6] G. Germano, H. Kiat, P. Kavanagh, M. Moriel, M. Mazzanti, H. Su, K. V. Train, D. Berman, Automatic quantification of ejection fraction from gated myocardial perfusion spect., *Journal of Nuclear Medicine* 36(11) (1995) 2138–47.
- [7] C. Cooke, E. Garcia, S. Cullom, T. Faber, R. Pettigrew, Determining the accuracy of calculating systolic wall thickening using a fast fourier transform approximation: a simulation study based on canine and patient data., *Journal of Nuclear Medicine* 35(7) (1994) 1185–92.
- [8] T. Miller, J. Wallis, B. Landy, R. Gropler, C. Sabharwal, Measurement of global and regional left ventricular function by cardiac pet, *Journal of Nuclear Medicine* 35(6) (1994) 999–1005.
- [9] K. Yamashita, N. Tamaki, Y. Yonekura, H. Ohtani, H. Saji, T. Mukai, H. Kambara, C. Kawai, T. Ban, J. Konishi, Quantitative analysis of regional wall motion by gated myocardial positron emission tomography: validation and comparison with left ventriculography., *Journal of Nuclear Medicine* 30(11) (1989) 1775–86.
- [10] I. Buvat, M. Bartlett, A. Kitsiou, V. Dilsizian, S. Bacharach, A “hybrid” method for measuring myocardial wall thickening from gated pet/spect images., *Journal of Nuclear Medicine* 38(2) (1997) 324–9.
- [11] C. C. Moore, C. H. Lugo-Olivieri, E. R. McVeigh, E. A. Zerhouni, Three-dimensional systolic strain patterns in the normal human left ventricle: Characterization with tagged mr imaging., *Radiology* 214 (2000) 453–466.
- [12] A. A. Amini, Y. Chen, R. W. Curwen, V. Manu, J. Sun, Coupled B-snake grids and constrained thin-plate splines for analysis of 2D tissue deformations from tagged MRI, *IEEE Transactions on Medical Imaging* 17:3 (1998) 344–356.
- [13] E. Haber, D. N. Metaxas, L. Axel, Motion analysis of the right ventricle from MRI images, in: *Medical Image Computing and Computer Aided Intervention (MICCAI)*, Cambridge, MA, 1998, pp. 177–188.
- [14] W. S. Kerwin, J. L. Prince, Cardiac material markers from tagged MR images, *Medical Image Analysis* 2 (4) (1998) 339–353.
- [15] J. Park, D. N. Metaxas, L. Axel, Analysis of left ventricular wall motion based on volumetric deformable models and MRI-SPAMM, *Medical Image Analysis* 1 (1) (1996) 53–71.

- [16] J. L. Prince, E. R. McVeigh, Motion estimation from tagged MR image sequences, *IEEE Transactions on Medical Imaging* 11 (1992) 238–249.
- [17] A. A. Young, D. L. Kraitchman, L. Dougherty, L. Axel, Tracking and finite element analysis of stripe deformation in magnetic resonance tagging, *IEEE Transactions on Medical Imaging* 14 (3) (1995) 413–421.
- [18] N. J. Pelc, Myocardial motion analysis with phase contrast cine MRI, in: *Proceedings of the 10th Annual SMRM, San Francisco, 1991*, p. 17.
- [19] J. S. Duncan, P. Shi, R. T. Constable, A. Sinusas, Physical and geometrical modeling for image-based recovery of left ventricular deformation, *Progress in Biophysics and Molecular Biology* 69 (2-3) (1998) 333–351.
- [20] F. G. Meyer, R. T. Constable, A. J. Sinusas, J. S. Duncan, Tracking myocardial deformation using phase contrast MR velocity fields: A stochastic approach, *IEEE Transactions on Medical Imaging* 15 (4).
- [21] Y. Zhu, M. Drangova, N. J. Pelc, Estimation of deformation gradient and strain from cine-PC velocity data, *IEEE Transactions on Medical Imaging* 16 (6).
- [22] S. Olaf, T. von Ramm, Real time volumetric ultrasound imaging system, *Journal of Digital Imaging* (1990) 261–266.
- [23] R. Lang, P. Vignon, L. Weinert, J. Bednarz, C. Korcarz, J. Sandelski, R. Koch, D. Prater, V. Mor-Avi, Echocardiographic quantification of regional left ventricular wall motion with color kinesis, *Circulation* 15;93(10) (1996) 1877–85.
- [24] M. Chuang, R. Parker, M. Riley, M. Reilly, R. Johnson, V. Korley, A. Lerner, P. Douglas, Three-dimensional echocardiography improves accuracy and compensates for sonographer inexperience in assessment of left ventricular ejection fraction, *J Am Soc Echocardiography* 12 (1999) 290–299.
- [25] M. Chuang, R. Beaudin, M. Riley, M. Mooney, W. Manning, M. Hibberd, P. Douglas, Impact of on-line endocardial border detection on determination of left ventricular volume and ejection fraction by transthoracic 3-dimensional echocardiography, *J Am Soc Echocardiography* 12 (1999) 551–558.
- [26] M. Chuang, M. Hibberd, C. Salton, R. Beaudin, M. Riley, R. Parker, P. Douglas, Importance of imaging method over imaging modality in non-invasive determination of left ventricular volumes and ejection fraction: Assessment by two- and three-dimensional echocardiography and magnetic resonance imaging, *J Am Coll Cardiology* 35 (2000) 477–484.
- [27] F. H. Sheehan, E. L. Bolson, R. W. Martin, G. Bashein, J. McDonald, Quantitative three dimensional echocardiography: Methodology, validation and clinical applications, in: *Medical Image Computing and Computer Aided Intervention (MICCAI)*, Boston, MA, 1998, pp. 102–109.
- [28] E. Angelini, A. Laine, S. Takuma, S. Homma, Directional representations of 4D echocardiography for temporal quantification of LV volume, in: *Medical Image*

- Computing and Computer Aided Intervention (MICCAI), Cambridge, England, 1999, pp. 430–440.
- [29] E. Brandt, L. Wigström, B. Wranne, Segmentation of echocardiographic image sequences using spatio-temporal information, in: Medical Image Computing and Computer Aided Intervention (MICCAI), Cambridge, England, 1999, pp. 410–419.
- [30] J. Montagnat, H. Delingette, G. Malandain, Cylindrical echocardiographic images segmentation based on 3D deformable models, in: Medical Image Computing and Computer Aided Intervention (MICCAI), Cambridge, England, 1999, pp. 168–175.
- [31] G. Jacob, A. Noble, M. Mulet-Parada, A. Blake, Evaluating a robust contour tracker on echocardiographic sequences, *Medical Image Analysis* 3 (1) (1999) 63–75.
- [32] K. Caidahl, E. Kazzam, J. Lingberg, G. N. Andersen, J. Nordanstig, S. R. Dahlqvist, A. Waldenstro, R. Wikh, New concept in echocardiography: harmonic imaging of tissue without use of contrast agent., *The Lancet* 352 (1999) 1264–1270.
- [33] T. R. Porter, F. Xie, A. Kricsfeld, A. Chiou, A. Dabestani, Improved endocardial border resolution using dobutamin stress endocardiography with intravenous sonicated dextrose albumin., *J. Am College of Cardiology* 23 (1994) 1440–43.
- [34] P. J. Hunter, A. McCulloch, P. Nielsen (Eds.), *Theory of heart*, Springer-Verlag, Berlin, 1991.
- [35] A. V. Panfilov, A. V. Holden (Eds.), *Computational Biology of the Heart*, John Wiley & Sons, 1997.
- [36] D. P. Dione, P. Shi, W. Smith, P. D. Man, J. Soares, J. S. Duncan, A. J. Sinusas, Three-dimensional regional left ventricular deformation from digital sonomicrometry, in: 19th Annual International Conference of the IEEE Engineering in Medicine and Biology Society, Chicago, IL, 1997, pp. 848–851.
- [37] D. Meoli, R. Mazhari, D. P. Dione, J. Omens, A. McCulloch, A. J. Sinusas, Three dimensional digital sonomicrometry: Comparison with biplane radiography, in: Proceedings of IEEE 24th Annual Northeast Bioengineering Conference, 1998, pp. 64–67.
- [38] X. Papademetris, J. V. Rambo, D. P. Dione, A. J. Sinusas, J. S. Duncan, Visually interactive cine-3D segmentation of cardiac MR images, *Suppl. to the J. Am. Coll. of Cardiology* 31 (2. Suppl. A).
- [39] A. Chakraborty, L. Staib, J. Duncan, Deformable boundary finding in medical images by integrating gradient and region information, *IEEE Transactions on Medical Imaging* 15 (6) (1996) 859–870.
- [40] C. de Boor, *A Practical Guide to Splines*, Springer-Verlag, New York, NY, 1978.

- [41] B. S. Manjunath, R. Chellappa, Unsupervised texture segmentation using markov random field models, *IEEE Transactions on Pattern Analysis and Machine Intelligence* 13 (1991) 478–482.
- [42] X. Papademetris, Estimation of 3D left ventricular deformation from medical images using biomechanical models, Ph. D. dissertation, Yale University, New Haven CT. (URL= <http://noodle.med.yale.edu/thesis>) (May 2000).
- [43] M. Mulet-Pabrada, J. A. Noble, 2D+T acoustic boundary detection in echocardiography, in: *Medical Image Computing and Computer Aided Intervention (MICCAI)*, Boston, MA, 1998, pp. 806–813.
- [44] P. Shi, A. J. Sinusas, R. T. Constable, E. Ritman, J. S. Duncan, Point-tracked quantitative analysis of left ventricular motion from 3D image sequences, *IEEE Transactions on Medical Imaging*, 19 (1) (2000) 36–50.
- [45] J. M. Guccione, A. D. McCulloch, Finite element modeling of ventricular mechanics, in: P. J. Hunter, A. McCulloch, P. Nielsen (Eds.), *Theory of Heart*, Springer-Verlag, Berlin, 1991, pp. 122–144.
- [46] L. E. Malvern, *Introduction to the Mechanics of a Continuous Medium*, Prentice-Hall, Englewood Cliffs, New Jersey, 1969.
- [47] T. J. R. Hughes, *The finite element method : linear static and dynamic finite element analysis*, Prentice-Hall, Englewood Cliffs, N.J., 1987.
- [48] D. Geman, S. Geman, Stochastic relaxation, Gibbs distribution and Bayesian restoration of images, *IEEE Transactions on Pattern Analysis and Machine Intelligence* 6 (1984) 721–741.
- [49] G. E. Christensen, R. D. Rabbitt, M. I. M. M. I., 3D brain mapping using deformable neuroanatomy, *Physics in Medicine and Biology* 39 (1994) 609–618.
- [50] J. C. Gee, D. R. Haynor, L. L. Briquer, R. K. Bajcsy, Advances in elastic matching theory and its implementation, in: *CVRMed-MRCAS*, Grenoble, France, 1997.
- [51] K. Bathe, *Finite Element Procedures in Engineering Analysis*, Prentice-Hall, New Jersey, 1982.
- [52] A. J. Sinusas, K. A. Trautman, J. D. Bergin, D. D. Watson, M. Ruiz, W. H. Smith, G. A. Beller, Quantification of area of risk during coronary occlusion and degree of myocardial salvage after reperfusion with technetium-99m methoxyisobutyl isonitrile., *Circulation* 82 (1990) 1424–37.
- [53] I. Hibbit, Karlsson & Sorencen, *Abaqus Version 5. 7*, Rhode Island, USA (1997).
- [54] P. Croissile, C. C. Moore, R. M. Judd., J. A. C. Lima, M. Arai, E. R. McVeigh, L. C. Becker, E. A. Zerhouni, Differentiation of viable and nonviable myocardium by the use of three-dimensional tagged MRI in 2-day-old reperfused infarcts., *Circulation* 99 (1999) 284–291.